EES Batteries

PAPER

View Article Online
View Journal

Cite this: DOI: 10.1039/d5eb00225g

Hybrid thermochemical Carnot battery with calcium looping, methane dry reforming, and supercritical carbon dioxide cycle: thermodynamic and techno-economic optimization

Jun Shen,[a] Yongqing Zhang,[a] Zihao Sun,[b] Dabiao Wang,[b] Sheng Li,[a] Wei Han,[c] Kezhen Zhang,[c] Xiao Yang,[c] Chenglong Yang[c] and Qianghui Xu *[a]

This study proposes a polygeneration hybrid thermochemical Carnot battery that integrates calcium-looping thermochemical storage with methane dry reforming in an electrically heated calciner, coupled to a supercritical CO_2 Brayton cycle for power discharge. Operating the calciner in a methane atmosphere lowers the calcination temperature by ~200 °C, mitigates sorbent deactivation, and enables *in situ* CO_2 utilization for synthesis-gas coproduction. A steady-state system model combined with multi-objective optimization is developed to examine efficiency–cost trade-offs. The Pareto-optimal compromise achieves a levelized cost of electricity (LCOE) of 0.94 ¥ per kWh, with a simplified recuperated cycle delivering 22.6 MW net output at a round-trip efficiency of 20.5%. Accounting for synthesis gas coproduct and ~90% CO_2 capture increases the overall energy and exergy efficiencies to 88.0% and 85.0%, respectively. Sensitivity analyses identify favorable operating windows of 30–50% CaO conversion and 5–10 °C minimum temperature approach in recuperators. Economies of scale are evident: as capacity expands from 1 to 100 MW, the LCOE declines from 2.37 to 0.83 ¥ per kWh. These findings demonstrate that incorporating methane dry reforming into calcium looping enables long-duration storage with inherent CO_2 capture and valuable syngas coproduction, offering attractive thermo-economic trade-offs for grid-scale applications.

Received 27th November 2025,
Accepted 6th March 2026

DOI: 10.1039/d5eb00225g

rsc.li/EESBatteries

Broader context

The global transition to carbon neutrality is critically dependent on solving two interconnected challenges: the large-scale integration of intermittent renewable energy through affordable long-duration storage, and the urgent need for decarbonizing industrial processes and chemical production. This study introduces a polygeneration Carnot battery that innovatively combines calcium-looping thermochemical energy storage with methane dry reforming and a supercritical CO_2 power cycle. By operating the calciner in a methane atmosphere, the system simultaneously achieves a significant reduction in the calcination temperature, mitigates sorbent deactivation, and enables *in situ* CO_2 utilization for syngas coproduction. The research demonstrates that this integrated approach not only provides a pathway for long-duration electricity storage with inherent CO_2 capture, but also transforms the storage system into a multi-product energy hub. The favorable thermo-economic trade-offs and clear economies of scale revealed by the analysis highlight the potential of this technology to enhance grid flexibility, promote a circular carbon economy, and offer a viable strategy for the synergistic decarbonization of the power and chemical sectors.

1. Introduction

Achieving net-zero emissions by 2050 will require a rapid scale-up of solar and wind generation, as projected by the International Energy Agency and the International Renewable Energy Agency.[1,2] Yet integrating these variable resources poses significant operational challenges: the temporal mismatch between generation and demand complicates unit commitment and dispatch,[3] driven by pronounced diurnal and seasonal variability.[4] Therefore, the advancement of carbon capture, utilization, and storage (CCUS) and power-to-X (PtX) technologies is critical for addressing grid stability and achieving low-carbon emissions.[5]

Carnot battery systems, considered a promising route for deep decarbonization, alleviate operational constraints of power-to-heat-to-power schemes by shifting electricity into a

[a]School of Mechanical Engineering, Beijing Institute of Technology, Beijing, 100081, P. R. China. E-mail: xuqh12@bit.edu.cn
[b]School of Mechanical Engineering and Automation, Fuzhou University, Fuzhou 350108, China
[c]Xi'an Thermal Power Research Institute Co., Ltd, Xi'an, 710032, China

thermal reservoir; however, when implemented with sensible or latent heat storage they still suffer from relatively low volumetric energy density—typically around or below 100 kWh m^{-3} for practical materials—along with cumulative thermal losses during long holding times and limited functional flexibility in matching discharge profiles to grid needs.[6–8] Thermochemical energy storage based on reversible reactions offers a compelling alternative with superior energy density approaching 500 kWh m^{-3}, theoretically indefinite storage duration, and temperature-independent energy transport capabilities.[9–11] Among these systems, calcium looping technology utilizing the reversible calcination–carbonation reaction of limestone stands out due to its ultra-high theoretical energy density of 889 kWh m^{-3}, natural abundance of limestone precursors, and intrinsic carbon capture potential during the carbonation phase.[12–14]

Since its proposal, $CaCO_3$/CaO cycling (CaL) systems have attracted significant research attention. Edwards *et al.*[15] pioneered an integrated system combining concentrating solar power, $CaCO_3$/CaO storage, and an open Brayton cycle, achieving 40–50% electrical efficiency with significantly reduced storage volume *versus* molten salt systems. Chacartegui *et al.*[12] integrated CaL with a closed CO_2 Brayton cycle, attaining over 45% efficiency through optimization. Ortiz *et al.*[16] demonstrated direct integration of CaL discharge with closed CO_2 cycles delivers optimal energy efficiency at 45–46%. Zhang *et al.*[17] enhanced a 50 MW Concentrated Solar Power (CSP) plant by integrating CaL thermochemical storage with PV-driven compressed CO_2 storage, doubling both energy efficiency from 14.6% to 29.4% and exergy efficiency from 15.7% to 31.6%, while achieving a levelized cost of electricity between $0.010 and $0.159 per kWh. Nevertheless, most CaL thermochemical storage and carbon capture integrations target CSP plants,[14] which incur high solar field investment costs and exhibit low-efficiency radiation heat transfer between compound parabolic concentrators and calcination reactors.[18] Therefore, this study directly employs electrical heating to meet the calcination reaction's energy demands and utilizes either coal-fired power plant steam Rankine cycles or Brayton cycles for energy discharge, establishing a novel CaL Carnot battery system for high-efficiency clean power generation.

Our previous study proposed a CaL Carnot battery integrated with a coal-fired power plant steam Rankine cycle.[19] By supplying high-temperature heat to partially replace the boiler reheater duty, the system reduced coal consumption by approximately 7.07% relative to the reference plant, achieved a round-trip efficiency of 36.93%, and realized a specific energy consumption for CO_2 capture of 3.66 MJ kg^{-1}. Nonetheless, two limitations remain: (i) the inherently high calcination temperature accelerates sorbent deactivation, undermining long-term capacity retention; and (ii) although lowering the reheater load curbs coal use and emissions, the configuration cannot deliver zero-emission operation while it remains coupled to a coal-fired unit—necessitating either full decoupling from fossil heat or complete capture of residual stack CO_2.

Simultaneously, Carnot battery systems based on calcium looping face progressive activity decay of calcium-based sorbents. Sun *et al.*[20] demonstrated that multi-cycle operation promotes CaO sintering, leading to pore coarsening and reduced sorbent conversion. Benitez-Guerrero *et al.*[21] revealed through microstructural analysis that rapid formation of dense $CaCO_3$ product layers under high-temperature, high-pressure CO_2 causes pore blockage and diffusion-limited reaction kinetics. To address sorbent deactivation, researchers have proposed several mitigation strategies, including: (i) recarbonation treatments to restore reactive surface area and slow sintering;[22,23] (ii) the use of additives or supports to stabilize the microstructure and sustain multi-cycle capacity;[24,25] and (iii) conducting calcination under a reducing atmosphere to suppress sintering and improve cyclic performance.[26,27] Notably, Shao *et al.*[28] reported that coupling calcium looping with dry reforming of methane enables calcination at 700 °C in a CH_4 atmosphere—approximately 200 °C lower than conventional operation—thereby markedly suppressing high-temperature sorbent deactivation. However, the consequences of this deactivation mitigation for system-level performance have yet to be systematically evaluated.

Building upon the aforementioned issues and prior work,[19] this study proposes an integrated hybrid thermochemical Carnot battery system coupling CaL thermochemical energy storage, dry reforming of methane, and a supercritical CO_2 Brayton cycle (CaL-DRM-sCO_2). The proposed system offers multifunctional benefits: accommodating surplus renewable electricity, enabling long-duration energy storage, capturing carbon, and co-producing synthesis gas (syngas) feedstock. Thermodynamic and economic models of the system were developed using Python. Key energy and economic performance metrics were defined, and a multi-objective optimization framework was established to identify Pareto-optimal trade-off solutions balancing efficiency and cost. The optimization results were evaluated through energy analysis, exergy analysis, and economic assessment to quantify system performance. Furthermore, the influence of key parameters on system behavior was investigated.

2. Models and methods

2.1 Integrated CaL-DRM-sCO_2 system

The charging subsystem of the proposed CaL-DRM-sCO_2 system is depicted in Fig. 1. The calciner is electrically heated using excess renewable electricity from the grid (a coal gasification module similar to those implemented in integrated gasification combined cycle (IGCC) systems). A stream of partially carbonated solids ($F_R - F_0$), comprising $CaCO_3$ and unreacted CaO (collectively termed '$CaCO_3$ + CaO'), exits the $CaCO_3$ storage tank and combines with a fresh limestone makeup stream (F_0) before entering the Heat Exchange Network (HEN). Simultaneously with limestone introduction, an equivalent molar flow (F_0) of circulating solids is purged from the $CaCO_3$ storage tank. This purge compensates for adsorbent de-

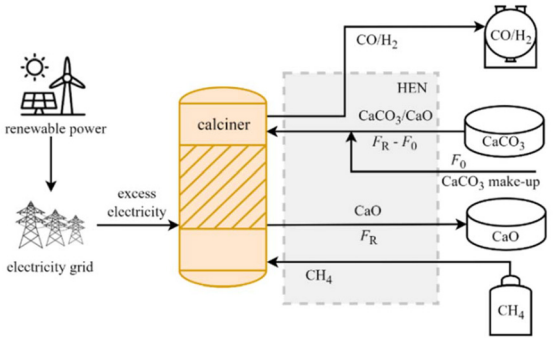

Fig. 1 Charging subsystem in the CaL-DRM-sCO_2 hybrid thermochemical Carnot battery system.

activation caused by high-temperature sintering and the decline in CO_2 capture capacity resulting from repeated carbonation/calcination cycles. Within HEN, the combined solid feed and the CH_4 stream (is assumed to be supplied *via* a dedicated gas pipeline), acting as cold streams, undergo thorough preheating prior to entering the calciner. Following calcination, the resulting CaO solids (F_R) and the syngas mixture, primarily CO and H_2, exit the calciner as hot streams. These hot streams then pass through HEN, transferring heat to preheat the incoming reactants while simultaneously cooling themselves. Subsequently, the cooled CaO solids and the cooled syngas mixture are separately conveyed to their respective storage tanks.

The proposed CaL-DRM-sCO_2 system distinguishes itself from the Calcium Looping integrated with a Coal-Fired Power Plant[19] (CaL-CPP) primarily through methane injection into the calciner. This enables calcination decomposition to proceed within a methane atmosphere, which achieves three synergistic effects: approximately 200 °C reduction in calcination temperature,[28] effective suppression of adsorbent thermal deactivation, and *in situ* reaction between released high-temperature CO_2 and CH_4. This integrated approach circumvents separate transportation and storage requirements for CO_2. The produced syngas, primarily comprising carbon monoxide and hydrogen, offers versatile downstream applications, notably serving as valuable feedstock for processes such as methanol synthesis and Fischer–Tropsch synthesis.[27] This syngas is generated *via* the governing reaction between carbon dioxide and methane, expressed as follows:

$$CO_2 + CH_4 \rightarrow 2CO + 2H_2 \quad \Delta H = +247\ \text{kJ mol}^{-1}. \qquad (1)$$

Collectively, the integrated reaction scheme within the calciner is governed by the following equation:

$$CaCO_3 + CH_4 \rightarrow CaO + 2CO + 2H_2 \quad \Delta H = +425\ \text{kJ mol}^{-1}. \qquad (2)$$

This study idealizes methane conversion as unity in order to decouple and highlight the thermochemical energy storage behavior of the $CaCO_3$/CaO system; however, this assumption may underestimate additional heat transfer losses or efficiency penalties arising from incomplete reforming. Fig. 2 illustrates the discharging subsystem of the CaL-DRM-sCO_2 hybrid thermochemical Carnot battery system. CaO solid particles are discharged from the storage tank, and CO_2-rich flue gas from plants (including but not limited to coal-fired power plants, cement plants, and steel mills) enter the carbonator reactor together after being preheated in the HEN. Within the carbonator, CaO reacts with CO_2 at approximately 650 °C through the carbonation reaction shown in:

$$CaO + CO_2 \rightarrow CaCO_3 \quad \Delta H = -178\ \text{kJ mol}^{-1}. \qquad (3)$$

This process converts the chemical energy of CaO solids into high-temperature heat while achieving approximately 90% carbon capture efficiency. The resulting partially carbonated solids, designated as $CaCO_3$ + CaO, and the decarbonized flue gas are subsequently cooled in HEN. During cooling, they transfer heat to the incoming CaO particles and CO_2-rich flue gas streams destined for the carbonator, thereby preheating these reactants. Critically, a key design feature involves direct heat transfer through the carbonator walls for thermal energy release during discharge. This integrated approach significantly simplifies HEN configuration on the carbonator side and enhances heat transfer efficiency compared to systems recovering heat from reaction products, yielding superior performance as demonstrated in ref. 29. Crucially, the substantial heat generated by the exothermic carbonation reaction is harnessed to drive a sCO_2 Brayton cycle for power generation. This cycle employs sCO_2 as the working fluid, leveraging its advantageous properties—notably high density akin to liquids and low viscosity like gases—which enable exceptional compressibility, efficient heat transfer, and excellent flow properties. For clarity, Fig. 2 presents a simplified schematic of the sCO_2 Brayton cycle configuration; detailed cycle design optimization is reserved for subsequent sections.

2.2 Simulation models

This study employs a steady-state process modeling framework to simulate mass and energy balances across all system components. A customized in-house thermodynamic program was developed to resolve the coupled heat transfer and chemical

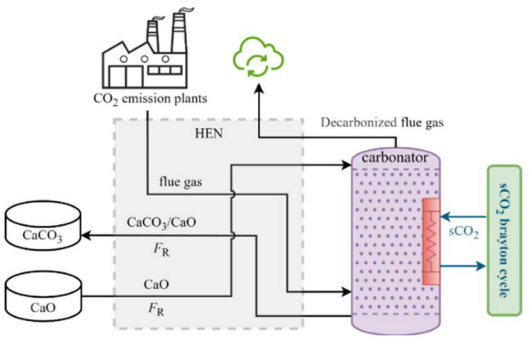

Fig. 2 Discharging subsystem in the CaL-DRM-sCO_2 hybrid thermochemical Carnot battery system.

reaction processes, ensuring numerical stability and convergence under varying operational conditions. Thermophysical properties of gaseous and liquid streams (*e.g.*, sCO_2, flue gas) were sourced from the NIST REFPROP database, while thermodynamic data for solid reactants (*e.g.*, CaO, $CaCO_3$) were obtained from the Aspen Plus® V11 property library. This dual-source approach guarantees consistency with widely accepted industrial standards.

Fig. 3 illustrates the mass balances of material streams within the CaL system. CaO enters the carbonator from the storage tank at a molar flow rate F_R. Within the carbonator, a portion of the incoming CaO undergoes carbonation, with the reacted molar flow designated as $F_{CaO,carb}$, and this process produces the same molar flow of $CaCO_3$ ($F_{CaCO_3,carb}$). Simultaneously, the unconverted CaO flow rate is designated $F_{CaO,unr,carb}$. Collectively, these molar flows thus satisfy the relationship:

$$F_{CaO,carb} = F_{CaCO_3,carb} = XF_R, \quad (4)$$

$$F_{CaO,unr,carb} = (1 - X)F_R. \quad (5)$$

Here, X represents the carbonation conversion of CaO. Critically, it should be emphasized that CaO and $CaCO_3$ physically coexist as indivisible composite particles – rather than discrete phases. The mass balance model's representation of CaO and $CaCO_3$ as separate fluid streams constitutes a deliberate idealization for computational tractability and conceptual clarity. The molar flow rate of CO_2-rich flue gas entering the carbonator is denoted $F_{flue\text{-}gas}$, the value of which is determined by:

$$F_{flue\text{-}gas} = \frac{XF_R}{\lambda y_{CO_2}}. \quad (6)$$

Here, λ denotes the CO_2 capture rate of the flue gas, and y_{CO_2} represents the mole fraction of CO_2 in the inlet flue gas. The molar flow rate of CO_2 participating in the carbonation reaction is calculated as:

$$F_{CO_2\text{-}capture} = XF_R. \quad (7)$$

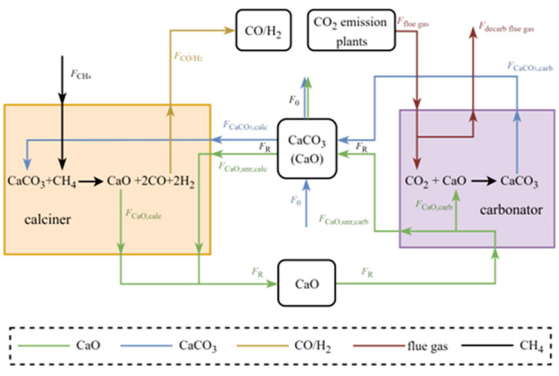

Fig. 3 Material streams of the CaL-DRM-sCO_2 system.

The molar flow rate of decarbonized flue gas exiting the carbonator is denoted $F_{decarb\text{-}flue\text{-}gas}$, the value of which is calculated as:

$$F_{decarb\text{-}flue\text{-}gas} = XF_R\left(\frac{1}{\lambda y_{CO_2}} - 1\right). \quad (8)$$

The total molar flow rate of solid particles exiting the carbonator is F_R. Fresh $CaCO_3$ is supplied to the $CaCO_3$ storage vessel at a molar flow rate F_0, and mixed particles ($CaCO_3$ + CaO) are simultaneously removed at molar flow rate F_0. The makeup ratio, r, is defined as the ratio of the fresh makeup flow rate F_0 to the total recirculating solid flow rate F_R, expressed as:

$$r = \frac{F_0}{F_R}, \quad (9)$$

its value is strongly dependent on the X, with the mathematical relationship expressed as:

$$X = \frac{a_1 f_1{}^2 r}{r + (1 - r)(1 - f_1)} + \frac{a_2 f_2{}^2 r}{r + (1 - r)(1 - f_2)} + b, \quad (10)$$

where the fitting constants in the deactivation equation for the base cycle are: $a_1 = 0.1045$, $f_1 = 0.9822$, $a_2 = 0.7786$, $f_2 = 0.7905$, and $b = 0.07709$.[30] However, these are not fixed parameters but were empirically derived by fitting the deactivation curve. Given the assumptions of a 1 : 1 charge/discharge duration ratio and complete decomposition of $CaCO_3$, the total molar flow rate of the mixed-particle stream exiting the $CaCO_3$ storage tank is denoted as F_R. Within this stream, the molar flow rate of the reactive $CaCO_3$ stream undergoing calcination in the calciner is denoted as $F_{CaCO_3,calc}$, which generates an equimolar flow of CaO ($F_{CaO,calc}$) through thermal decomposition. These values are calculated as follows:[14]

$$F_{CaCO_3,calc} = F_{CaO,calc} = X(F_R - F_0) + F_0, \quad (11)$$

the molar flow rate of the non-reactive CaO stream calcination is $F_{CaO,unr,calc}$, which is calculated as:

$$F_{CaO,unr,calc} = (F_R - F_0)(1 - X). \quad (12)$$

During cyclic operation, two types of solid particles enter the calciner: partially carbonated particles with a CaO core and a $CaCO_3$ outer layer, and freshly supplied $CaCO_3$ particles. In the calciner, $CaCO_3$ is assumed to undergo complete decomposition; the $CaCO_3$ layer of the partially carbonated particles is fully converted to CaO, and the fresh $CaCO_3$ particles are also entirely transformed into CaO. As a result, only CaO particles exit the calciner, with a total molar flow rate denoted as F_R.

It should be noted that the solid particles exiting the calciner consist exclusively of CaO, with a total molar flow rate of F_R. CH_4 at a molar flow rate of F_{CH_4} enters the calciner where it reacts to produce syngas (CO/H_2), with the combined molar flow rate denoted as F_{CO/H_2}. The inlet and outlet gaseous molar flow rates for the calciner are, respectively:

$$F_{CH_4} = X(F_R - F_0) + F_0, \quad (13)$$

$$F_{CO/H_2} = 4X(F_R - F_0) + 4F_0. \quad (14)$$

Carbon deposition *via* methane cracking and the Boudouard reaction is a known operational risk in dry reforming systems. In practical operation, these effects can be effectively mitigated by maintaining an appropriate CH_4/CO_2 feed ratio, operating at sufficiently high temperatures, and, where necessary, introducing limited amounts of steam. Such measures are commonly adopted to suppress carbon formation without fundamentally altering the system configuration. In the present study, these mitigation strategies are assumed to be in place, and carbon deposition is therefore not explicitly modeled at the system level.

The design parameters for the calcium looping section of the CaL-DRM-sCO_2 system are specified in Table 1. Parameters for the carbonator side follow ref. 19 and are not listed separately herein.

The hybrid thermochemical Carnot battery system employs an intercooled recompression sCO_2 Brayton cycle as the power block during discharge. Building upon this baseline configuration, a reheating process is implemented between the two turbines to enhance cycle efficiency and reduce turbine operating pressures and temperatures. The finalized cycle layout and key design parameters are presented in Table 2 and Fig. 4. An optional waste heat heater can be strategically positioned within this configuration between the high-temperature recuperator (HTR) and the low-temperature recuperator (LTR). This heater utilizes industrial waste heat to elevate the temperature of the sCO_2 working fluid exiting the LTR, bringing it closer to the inlet temperature requirement of the HTR, thereby optimizing thermal matching across the recuperative heat exchange process.

All reactors in the system are treated as zero-dimensional open reacting systems for the present analysis, while detailed reactor configurations and spatially resolved designs are currently under active investigation. In the ongoing engineering studies, the reactors are primarily being developed based on fixed-bed or moving-bed concepts, with their specific hydrodynamics, heat transfer characteristics, and scalability addressed in dedicated follow-up work. Consequently, chemical reaction kinetics are excluded from their thermodynamic modeling. The system energy and exergy balance equations are summarized in Tables 3 and 4, with detailed methodologies available in ref. 11, 14 and 19.

Table 1 Parameters for the calcium looping section of the CaL-DRM-sCO_2 system

Parameters	Components/ streams	Values
Calciner temperature	Calciner	700 °C (ref. 28)
Standard enthalpy of reaction	Calciner	425 kJ mol^{-1}
Thermal loss	Calciner	4%
Pressure loss	Calciner	15 kPa (ref. 31)
	CH_4	1% [14]
	CO/H_2 syngas	2% [14]
Minimum temperature difference	HENs	15 °C (ref. 11)
Specific electrical work of solid conveying	CaO, $CaCO_3$	10 kJ (kg 100 m)$^{-1}$ (ref. 32)
Storage vessel-calciner distance	CaO, $CaCO_3$	100 m (ref. 32)
Isentropic efficiency	Fan	80% [29]
Mechanical efficiency	Fan	97% [32]
Heat transfer coefficient	Gas	600 W (m^2 K)$^{-1}$ (ref. 14)
	Solid particle	200 W (m^2 K)$^{-1}$ (ref. 14)
Heat discharge	Carbonator	40 MW
Annual operating time	Calciner	2922 h
	Carbonator	2922 h

Table 2 Parameters of sCO_2 Brayton cycle

Parameters	Components/ streams	Values
Heat source temperature	Carbonator	650 °C (ref. 33)
Minimum temperature	sCO_2	32 °C
Waste heat exhaust temperature	Waste heat exhaust gas	200 °C
Isentropic efficiency	Compressor	88% [29]
	Turbine	92% [29]
Mechanical efficiency	Compressor/turbine	98% [29]
Minimum pressure	sCO_2	7.5 MPa (ref. 29)
Minimum pinch point temperature	Heater/recuperator	10 °C
Heat exchanger thermal loss		1% [34]

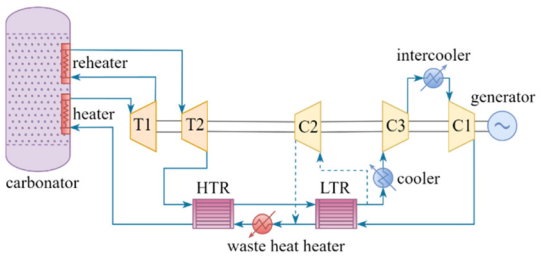

Fig. 4 Configuration of sCO_2 Brayton cycle.

Table 3 Energy balance models

Components/ processes	Governing equations
Reactors	$F_{CaO}\Delta H_R(T_{react}) + \sum m_{i,in}[h_i(T_{react}) - h_i(T_{in})] = \Phi$
	$\Delta H_R(T_{react}) = \Delta H_R^{0,i} + \sum_i \nu_i \int_{T_{ref}}^{T_{react}} c_{p,i} dT$
Heat exchanger	$c_{p,hot} m_{hot}(T_{hot,in} - T_{hot,out}) = c_{p,cold} m_{cold}(T_{cold,out} - T_{cold,in})$
	$T_{mix} = \frac{m_1 T_1 + m_2 T_2}{(m_1 + m_2)}$
Turbomachinery	$W_C = \frac{m_{sCO_2}(h_{out,C} - h_{in,C})}{\eta_{is,C}\eta_{m,C}}$
	$W_T = m_{sCO_2}(h_{in,T} - h_{out,T})\eta_{is,T}\eta_{m,T}$

Table 4 Exergy models

Component/process	Governing equations
Exergy (work/heat)	$E_{x,W} = W$ $E_{x,Q} = Q\left(1 - \frac{T_0}{T_Q}\right)$
	$E_x = E_{x,phys} + E_{x,chem} + E_{x,kin} + E_{x,pote}$
	$E_{x,phys} = (H - H_0) - T_0(S - S_0)$
Chemical exergy	$E_{x,chem} = n\sum_i x_i E^0_{x,i} + nRT_0\sum_i x_i \ln(x_i)$
	$E^0_x(A_aB_bC_c) = \Delta G^\circ(A_aB_bC_c) + aE^0(A) = bE^0(B) + cE^0(C)$
Exergy destruction	$I_{HEX} = E_{x,hot,in} + E_{x,cold,in} - E_{x,hot,out} - E_{x,cold,out}$
	$I_{calc} = E_{x,elec} + \Delta E_{x,H,calc} + \Delta E^0_{x,calc}$
	$I_{carb} = -E_{x,Q} + \Delta E_{x,H,carb} + \Delta E^0_{x,carb}$

Investment cost constitutes a critical factor in assessing the techno-economic feasibility of the system, primarily comprising two components: the Total Plant Cost (TPC) and the Total Annualized Cost (TAC). The TPC is defined as follows:[31]

$$TPC = i_{TASC}[(1 + i_{LC} + i_{E\&PC})(1 + i_{P\&C})\sum IC_i], \quad (15)$$

where i_{TASC} denotes the total as-spent cost multiplier at a value of 1.12, i_{LC} represents the construction labor cost indicator at 0.27, $i_{E\&PC}$ signifies the engineering and project cost indicator at 0.18, and $i_{P\&C}$ indicates the piping and integration cost indicator at 0.03,[14] which primarily accounts for ancillary construction-phase expenses, including management, administration, risk, and uncertainties. The total equipment cost $\sum IC_i$(¥) comprises the sum of individual component costs throughout the system, including but not limited to the calciner, carbonator, heat exchangers, fans, compressors, turbines, and coolers.

Reactors are configured as circulating fluidized-bed reactors (CFBRs). This design promotes intensive gas–solid contact under fluidization regimes, thereby enhancing reaction rates. The cost function for the calciner is defined as follows:[33]

$$IC_{calc} = 1\,831\,151 Q_{calc}^{0.65}, \quad (16)$$

where Q_{calc} denotes the thermal energy input to the calciner (MW). Similarly, the cost function for the carbonator is defined as follows:[35]

$$IC_{carb} = 133\,671 Q_{carb}^{0.5}, \quad (17)$$

where Q_{carb} denotes the thermal energy input to the carbonator (MW). The cost function for the HENs is defined according to:[31]

$$IC_{HEX} = 20\,409 A_{HEX}^{0.67} p_{HEX}^{0.28}, \quad (18)$$

where p_{HEX} denotes the operating pressure of the heat exchanger (bar), and A_{HEX} represents its heat transfer area (m^2), as determined by the following expression:

$$A_{HEX} = \frac{Q_{HEX}}{U\Delta T_{lm}}, \quad (19)$$

where Q_{HEX} denotes the heat duty of the exchanger (W), U represents the overall heat transfer coefficient (W $(m^2\ K)^{-1}$) governed by the heat transfer fluid properties, and ΔT_{lm} is the logarithmic mean temperature difference (LMTD, K). Similarly, the cost function for fans is defined as follows:[31]

$$IC_{fan} = 826\,934\left(\frac{P_{fan}}{445}\right)^{0.67}, \quad (20)$$

where P_{fan} represents the fan power draw (kW).

Within the sCO_2 Brayton cycle architecture, the compressor cost correlation adopts:[36]

$$IC_{comp} = 8\,917\,503 W_{comp}^{0.3992}, \quad (21)$$

where W_{comp} denotes the compressor power consumption (MW). The cost function for the turbine in the sCO_2 Brayton cycle is given by:[36]

$$IC_{turb} = 1\,323\,850 W_{turb}^{0.5561} f_{T,turb}, \quad (22)$$

where W_{turb} denotes the turbine power consumption (MW), and $f_{T,turb}$ denotes the temperature-dependent performance correction factor for the turbine, calculated as follows:

$$f_{T,turb} = \begin{cases} 1 & T_{max,turb} < 550 \\ 1 + 1.106 \times 10^{-4}(T_{max,turb} - 550)^2 & T_{max,turb} \geq 550 \end{cases}, \quad (23)$$

where $T_{max,turb}$ represents the turbine inlet temperature limit (°C). For the sCO_2 Brayton cycle recuperator subsystem, the cost correlation adopts:[36]

$$IC_{recup} = 359(UA_{recap})^{0.7544} f_{T,recup}, \quad (24)$$

where the $f_{T,recup}$ is the temperature-dependent performance correction factor, determined by:

$$f_{T,recup} = \begin{cases} 1 & T_{max,recup} < 550 \\ 1 + 0.02141(T_{max,recup} - 550)^2 & T_{max,recup} \geq 550 \end{cases}, \quad (25)$$

where $T_{max,recup}$ denotes the peak operating temperature of the recuperator (°C).

Regarding the main heater in the CO_2 Brayton cycle, its cost model follows Carlson *et al.*,[37] which is calculated *via* eqn (26):

$$IC_{abs} = UA_{abs} c_{abs}, \quad (26)$$

where c_{abs} denotes the normalized cost coefficient (¥ per (W per K)), specifically calculated through linear interpolation between discrete data points of corresponding *UA* values. The reference cabs values for *UA* interpolation are listed in Table 5.

The cost function for the cooler in the CO_2 Brayton cycle is given by:[31]

$$IC_{cooler} = 258.8 Q_{cooler}, \quad (27)$$

where Q_{cooler} denotes the heat duty of the cooler (kW). The cost function for the electric generator is given by:[36]

$$IC_{EG} = 789\,525 P_{EG}^{0.5463}, \quad (28)$$

Table 5 Normalized specific cost of the main heater for data interpolation

UA_{abs} (W K^{-1})	c_{abs} (¥ per (W per K))
5×10^3	13.78
3×10^4	9.43
1×10^5	7.98
3×10^5	7.25
1×10^6	7.25

where P_{EG} denotes the rated electrical power output of the generator (MW).

The net annual operating cost (TAC) is defined as follows:[31]

$$\mathrm{TAC} = (i_{OLC} + i_{MC})\mathrm{TPC} + \mathrm{AC}_{limestone} + \mathrm{AC}_{methane} + \mathrm{AC}_{elec} - \mathrm{AR}_{capture} - \mathrm{AR}_{syngas}, \quad (29)$$

where i_{OLC} denotes the annual operating labor cost indicator (adopted as 0.006 in this study), i_{MC} represents the maintenance cost indicator (0.0125), $\mathrm{AC}_{methane}$ is the annual CH_4 supply cost at a unit price of 4 ¥ per kg, and AC_{elec} signifies the annual renewable electricity cost at 0.165 ¥ per kWh. And the annual CO_2 capture revenue $\mathrm{AR}_{capture}$ is valued at 200 ¥ per t, while syngas revenue AR_{syngas} is set at 1.07 ¥ per kg. $\mathrm{AC}_{limestone}$, denotes the annual limestone replacement cost and is evaluated using a hypothetical unit price that scales exponentially with the CaO conversion X (Fig. 5). This functional form is adopted as a modeling assumption to assess economic sensitivity, rather than as an empirically validated correlation.

2.3 Technical assessments

This study adopts multiple performance metrics to evaluate the proposed integrated system. Among these, round-trip efficiency serves as the fundamental metric for assessing hybrid thermochemical Carnot battery performance, defined as:

$$\eta_{RT} = \frac{W_{EG}}{\sum W_i} \times 100\%, \quad (30)$$

where W_{EG} is the system's net electrical output (MW), and $\sum W_i$ represents the total energy input to the system (MW). This includes excess electrical energy supplied to the calciner and auxiliary power consumption from supporting equipment (*e.g.*, solid conveyors, blowers, compressors). The hybrid thermochemical Carnot battery system achieves effective CO_2 capture during the discharge process. Therefore, using round-trip efficiency alone provides a partial perspective for system evaluation. To holistically assess performance, we define an integrated system efficiency that incorporates the benefit of CO_2 capture, expressed as:

$$\eta_C = \frac{W_{EG}}{\sum W_i - \frac{F_{CO_2\text{-capture}} W_{CO_2\text{-capture,ideal}}}{1 \times 10^6}} \times 100\%, \quad (31)$$

where $F_{CO_2\text{-capture}}$ denotes the molar flow rate of captured CO_2 (mol s^{-1}), and $W_{CO_2\text{-capture,ideal}}$ represents the ideal energy consumption per mole of CO_2 captured (J mol^{-1}), *i.e.*, the minimum separation work. This is calculated as follows:

$$W_{CO_2\text{-capture,ideal}} = RT_{flue\text{-}gas}\left(\sum y_{out,i} \ln(y_{out,i}) - \sum y_{in,i} \ln(y_{in,i})\right), \quad (32)$$

where $T_{flue\text{-}gas}$ denotes the flue gas temperature (K), and $y_{in,i}$, $y_{out,i}$ represent the mole fractions of gas component i in the flue gas before and after the carbonation reaction, respectively.

For the CaL-DRM-sCO_2 system, the energy outputs comprise electrical power generation (W_{EG}) and the chemical energy of syngas ($E_{chem,syngas}$). The energy inputs include the total electrical energy input ($\sum W_i$), chemical energy of consumed methane (E_{chem,CH_4}), and industrial waste heat ($Q_{waste\text{-}heat}$). Thus, the energy efficiency of the CaL-DRM-sCO_2 system is derived as:

$$\eta_{En,CDs} = \frac{W_{EG} + E_{chem,syngas}}{\sum W_i + E_{chem,CH_4} + Q_{waste\text{-}heat}}. \quad (33)$$

Similarly, the exergy outputs include the exergy of net electrical output ($E_{x,W_{EG}}$) and chemical exergy of syngas ($E_{xchem,syngas}$), while exergy inputs comprise the exergy of electrical input (E_{x,W_i}), chemical exergy of methane feed ($E_{x,chem,CH_4}$), and exergy of industrial waste heat ($E_{x,Q_{waste\text{-}heat}}$). Thus, the exergy efficiency of the CaL-DRM-sCO_2 system is defined as:

$$\eta_{Ex,CDs} = \frac{E_{x,W_{EG}} + E_{x,chem,syngas}}{E_{x,W_i} + E_{x,chem,CH_4} + E_{x,Q_{waste\text{-}heat}}}. \quad (34)$$

The specific energy consumption per unit CO_2 captured (SEC) serves as a key metric for evaluating the system's carbon capture capability. With units of MJ kg^{-1}, it is defined as:

$$W_{CO_2} = \frac{\sum W_i - W_{EG}}{m_{CO_2\text{-capture}}}, \quad (35)$$

where $m_{CO_2\text{-capture}}$ denotes the system's continuous CO_2 capture rate (kg s^{-1}).

Additionally, this study employs the levelized cost methodology to evaluate electricity costs. This approach integrates the system's TPC, TAC, and discount rate over its operational life-

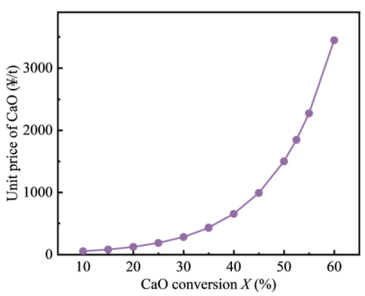

Fig. 5 Exponential scaling of limestone unit price with CaO conversion (X).

time. The levelized cost of electricity (LCOE), expressed in ¥ per kWh, is defined as:

$$\mathrm{LCOE} = \frac{\mathrm{TPC} + \sum_{i=1}^{k} \frac{\mathrm{TAC}}{(1+r)^i}}{\sum_{i=1}^{k} \frac{E_{\mathrm{output}}}{(1+r)^i}}, \quad (36)$$

where i denotes the current operating year, k represents the plant's operational lifetime (adopted as 30 years in this work), and r is the discount rate (set at 6% herein). E_{output} signifies the annual electricity output (kWh). Complementary to this economic framework, the Internal Rate of Return (IRR) serves as a pivotal metric for evaluating investment profitability and feasibility. This rate is defined as the discount rate at which the Net Present Value (NPV) of the investment project equates to zero, determined iteratively through:

$$\mathrm{NPV} = -\mathrm{TPC} + \sum_{i=1}^{k} \frac{\mathrm{AR} - \mathrm{TAC}}{(1+\mathrm{IRR})^i} = 0, \quad (37)$$

where AR denotes the Annual Revenue from electricity sales (¥). Crucially, a higher IRR value indicates stronger investment profitability, demonstrating a direct correlation between this metric and project attractiveness. The $C_{\mathrm{CO_2\text{-}capture}}$, expressed in ¥ per t, quantifies the operating cost required to capture one tonne of CO_2. It is calculated as:

$$C_{\mathrm{CO_2\text{-}capture}} = \frac{\mathrm{TAC}}{3.6 m_{\mathrm{CO_2\text{-}capture}} t_{\mathrm{year}}}, \quad (38)$$

where t_{year} represents the system's annual operating hours (h).

2.4 Optimization method

This study conducts multi-objective optimization of the CaL-DRM-sCO_2 system using the NSGA-II algorithm, where the defined objective functions (Table 6) comprise exergy efficiency maximization for energy performance and LCOE minimization for economic performance. These conflicting objectives necessitate a balanced compromise solution. Consequently, the configuration closest to the exergy efficiency midpoint within the Pareto frontier is selected as the optimal trade-off solution to reconcile thermodynamic and economic trade-offs.

The decision variables and their parametric boundaries for the multi-objective optimization model are detailed in Table 7, with the CaO conversion (X) – a performance-dominant parameter in the energy storage subsystem – selected as the primary decision variable for storage optimization. For the discharging subsystem, critical decision variables include the sCO_2 Brayton cycle's maximum pressure (p_{H}), intermediate turbine pressure (p_{MH}), intermediate compressor pressure (p_{ML}), and compression flow split ratio (β) – the latter defined as the mass flow ratio of sCO_2 entering the main compressor (C1) to the total working fluid mass flow according to eqn (39).

$$\beta = \frac{m_{\mathrm{sCO_2,C1}}}{m_{\mathrm{sCO_2,total}}}. \quad (39)$$

The constrained parameters in this multi-objective optimization include the main compressor outlet temperature ($T_{\mathrm{C1,out}}$), waste heat recuperator thermal load (Q_{WH}), cold stream outlet temperatures of the LTR and HTR ($T_{\mathrm{LTR,cold,out}}$/$T_{\mathrm{HTR,cold,out}}$), and HEN hot utility for the carbonator side ($Q_{\mathrm{hot\text{-}utility}}$), as tabulated in Table 8. The constraint principles fundamentally derive from thermodynamic imperatives: the main compressor outlet temperature (defining the cycle minimum temperature) must exceed the sCO_2 threshold at ≥32 °C, while the waste heat recuperator thermal load is constrained to non-negative values ensuring unidirectional heat transfer. Furthermore, recuperator temperature differences are governed by the second law's irreversibility requirement, mandating cold-stream outlet temperatures to remain below hot-stream inlets minus the 10 °C pinch point difference. Additionally, the absence of auxiliary heating for the carbonator subsystem necessitates zero hot utility consumption in HEN.

Furthermore, the population size and parameter configuration for the NSGA-II algorithm are specified in Table 9.

Table 6 Optimization objectives and objective functions of the CaL-DRM-sCO_2 system

Optimization objectives	Objective functions
Energy performance	Max. $\eta_{\mathrm{Ex,CDs}}$
Economic performance	Min. LCOE

Table 7 Decision variables for the CaL-DRM-sCO_2 system

Decision variables	Lower bounds	Upper bounds
X	10%	70%
p_{H}	20 MPa	30 MPa
p_{MH}	10 MPa	18 MPa
p_{ML}	8 MPa	15 MPa
β	0	1

Table 8 Optimization problem's constraints

Parameters	Constraint conditions
$T_{\mathrm{C1,out}}$	≥32 °C
Q_{WH}	≥0
$T_{\mathrm{LTR,cold,out}}$	≤$T_{\mathrm{LTR,hot,in}}$ − 10 °C
$T_{\mathrm{HTR,cold,out}}$	≤$T_{\mathrm{HTR,hot,in}}$ − 10 °C
$Q_{\mathrm{hot\ utility}}$	=0

Table 9 Algorithm parameters

Parameters	Values
Population size	60
Generations	80
Crossover probability	0.95
Mutation probability	0.9

3. Validation

The credibility of the proposed hybrid thermochemical Carnot battery system is established through component-level validation. The operational reliability of the core reversible Brayton cycle (compressor, turbine, heat exchangers) was confirmed by our prior experimental work[11,19,38] and benchmarking against literature data. The designs for the heat exchanger network and reactor are adopted from ref. 14.

Furthermore, the system's cost models are grounded in industrial data: component costs for the supercritical CO_2 cycle are derived from 4–24 supplier quotations,[36] while costs for the heat network and reactor are sourced from ref. 14. By integrating these proven performance data and credible cost models, the overall system analysis presented here is highly reliable.

4. Results and discussion

4.1 System optimization results

As illustrated in Fig. 6, the Pareto frontier obtained through multi-objective optimization reveals a pronounced trade-off relationship between LCOE and exergy efficiency. When LCOE decreases from approximately 1.106 ¥ per kWh to 0.916 ¥ per kWh, the system's exergy efficiency increases from 84.70% to 85.36%, indicating that pursuing higher energy efficiency incurs higher economic costs, and *vice versa*. The distribution of non-dominated solutions demonstrates a nonlinear correlation between these objectives: within the exergy efficiency range of 84.70–85.50%, LCOE increases marginally by only 0.006 ¥ per kWh per 0.1% efficiency gain, suggesting a favorable compromise zone between economy and performance. Conversely, beyond 85.0% exergy efficiency, each 0.1% improvement requires a steep LCOE increment of 0.048 ¥ per kWh, causing drastic economic deterioration. Consequently, the non-dominated solution closest to the exergy efficiency midpoint within the Pareto set is selected as the optimal compromise, with corresponding decision variables and objective values detailed in Table 10. Notably, the compression β of 1 indicates the reversion from the recompression Brayton cycle configuration to a simple recuperated cycle topology, eliminating the need for working fluid splitting and inter-stage compression.

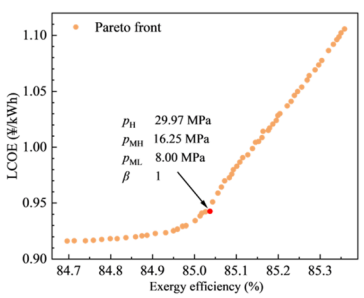

Fig. 6 Multi-objective optimization results for the CaL-DRM-sCO_2.

Table 10 Decision variables and objective function values of the optimal solution

	Parameters	Result
Objective function values	Exergy efficiency	85.03%
	LCOE	0.94 ¥ per kWh
Decision variables	X	48.74%
	p_H	29.97 MPa
	p_{MH}	16.25 MPa
	p_{ML}	8.00 MPa
	β	1

Fig. 7 shows the energy and exergy analyses of the baseline case, which is the optimal trade-off solution obtained through multi-objective optimization. Producing 22.57 MW of electrical power requires a significant combined input of surplus and auxiliary electrical energy totaling 110.25 MW. This high demand mainly comes from the calciner, where simultaneous calcination and CH_4 dry reforming reactions greatly increase its energy needs. As a result, the system has a relatively low electrical round-trip efficiency of 20.47%. However, relying only on round-trip efficiency to assess system performance has limitations. During the charging phase, the system produces valuable syngas as a co-product, while the discharging phase captures carbon with a capacity of 8.41 MJ kg^{-1}. Including these polygeneration benefits results in much higher overall system efficiencies: 88.04% on an energy basis and 85.03% on an exergy basis.

Fig. 7(a) depicts the energy flow diagram for the baseline case. Total system input energy reaches 331.67 MW, comprising surplus electricity (107.87 MW), auxiliary power consump-

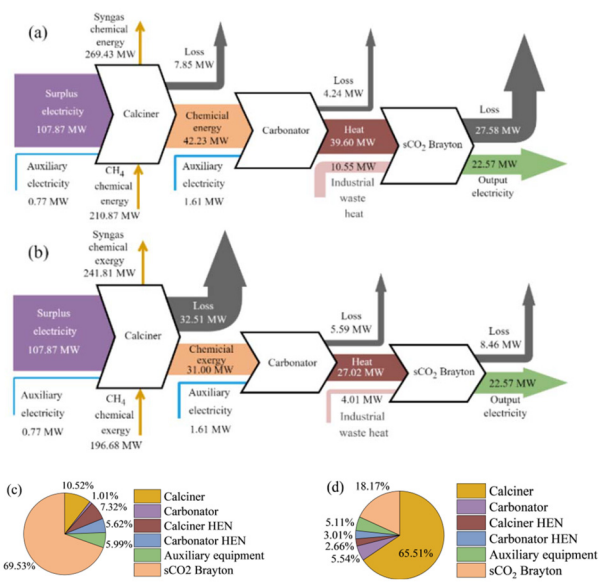

Fig. 7 Energy and exergy analyses of the baseline CaL-DRM-sCO_2 system: (a) energy flow diagram; (b) exergy flow diagram; (c) energy loss diagram; (d) exergy destruction diagram.

tion (2.38 MW), CH_4 chemical energy (210.87 MW), and industrial waste heat (10.55 MW). Total output energy is 292.00 MW, consisting of generated electricity (22.57 MW) and syngas chemical energy (269.43 MW). Within the calciner, a portion of the input surplus electricity is converted and stored as chemical energy within CaO solid particles (42.23 MW). During subsequent energy discharge, the stored chemical energy in CaO is released as 39.60 MW of thermal energy within the carbonator. This thermal energy heats the sCO_2 working fluid, ultimately driving the sCO_2 Brayton cycle to generate 22.57 MW electrical output. Fig. 7(c) details the distribution of energy losses. Irreversible thermal and mechanical losses within the sCO_2 Brayton cycle dominate, accounting for 69.53% of the total energy dissipation. These are followed by heat losses from the HEN (5.13 MW) and thermal losses from the two reactors (4.59 MW). Auxiliary power consumption includes energy for solids transport (1.30 MW) and fan operation (1.08 MW).

Fig. 7(b) depicts the exergy flow diagram for the baseline case. Total exergy input reaches 310.94 MW, comprising exergy of surplus electricity (107.87 MW), parasitic exergy consumption (2.38 MW combined), chemical exergy of methane (196.68 MW), and exergy of industrial waste heat (4.01 MW). Total exergy output is 264.38 MW, including generated electricity exergy (22.57 MW) and chemical exergy of syngas (241.81 MW). Within this flow, 31.00 MW of electrical exergy is converted and stored as chemical exergy in CaO. During discharge, this stored chemical exergy transforms into 27.02 MW of thermal exergy *via* carbonation, ultimately driving the Brayton cycle to produce 22.57 MW of electrical output. Fig. 7(d) details the distribution of exergy destruction. The calciner dominates exergy destruction at 65.51%, primarily due to significant energy-grade degradation during electrical-to-thermal conversion. The Brayton cycle contributes substantially less to exergy loss (18.17%) than energy loss, attributable to the low-grade exergy of the discharged low-pressure sCO_2 from the compressor.

Economic analysis of the baseline case reveals a TPC of 295.34 million CNY (M¥), with the cost structure detailed in Fig. 8(a). Equipment expenditure dominates at 176.56 M¥, constituting 59.78% of TPC. As labor, engineering, piping/integration, and miscellaneous costs scale proportionally with equipment investment, the latter represents the primary cost driver. Fig. 8(b) details the equipment cost breakdown, identifying five major components: the calciner (38.38 M¥; 21.74% of total equipment costs), carbonator (26.73 M¥), recuperator (28.31 M¥), turbine (21.43 M¥), and compressor (20.95 M¥). Collectively, these components represent 76.91% of equipment expenditure, with the calciner constituting the largest individual share. Notably, the sCO_2 Brayton cycle's recuperator incurs higher relative costs than the entire HEN in the calcium looping system, attributable to stringent material and sealing requirements under high-pressure operating conditions.

Fig. 9 shows the cost and revenue breakdown within the TAC framework. CH_4 consumption dominates operational expenses at 71.87%, driven by high calciner demand that requires a continuous input of 13.64 t h^{-1} during charging.

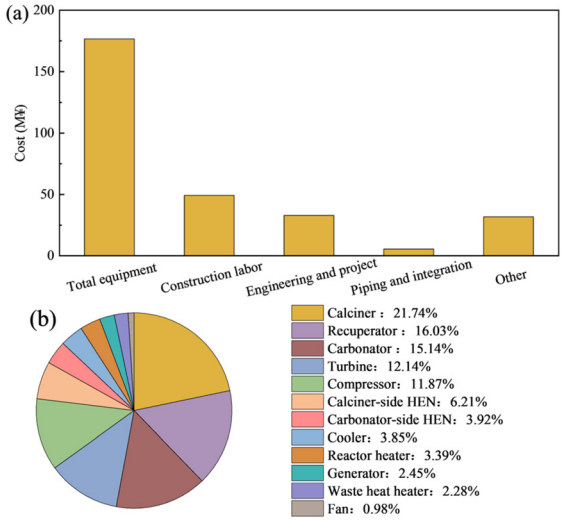

Fig. 8 Economic analysis of the baseline CaL-DRM-sCO_2 system: (a) TPC breakdown; (b) equipment cost breakdown.

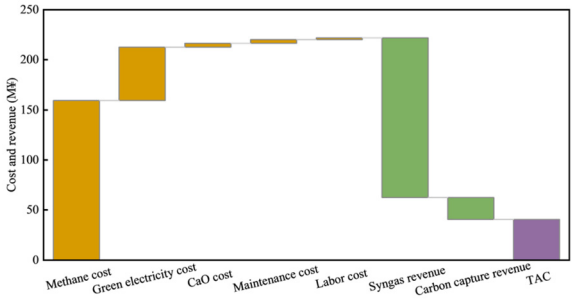

Fig. 9 Annual net operating cost analysis.

Green electricity accounts for a significant 23.96% due to the calciner's high power needs, while CaO, maintenance, and labor costs remain small. Conversely, syngas sales provide the main revenue stream (159.45 M¥), supported by carbon capture credits (21.92 M¥). The net economic assessment results in a TAC of 40.48 M¥ after balancing costs and revenue.

4.2 Sensitivity analysis

The Pareto-optimal trade-off solution derived from multi-objective optimization was selected as the baseline scenario for the system, accounting for the uncertainties in system design parameters and the potential for optimizing both energetic and economic performance. A sensitivity analysis is conducted to evaluate the impact of fluctuations in key parameters on the performance of this baseline system. This analysis focuses on four critical parameters: the CaO conversion rate, the minimum temperature (ΔT_{min}) in heat exchangers, the system scale, and the annual operating hours. The objective is to investigate their sensitivity to system performance metrics, particularly energy efficiency and economic indicators, thereby

identifying stable operational boundaries and potential for further optimization.

4.2.1 Effects of CaO conversion rate. The CaO conversion rate X is a crucial factor influencing the energy and economic performance of the CaL-DRM-sCO_2 system. Fig. 10 illustrates the resultant r under three operational scenarios: the base case without any sorbent treatment, the recarbonation-assisted process, and the CH_4-driven calcination process, to assess how the sorbent deactivation mitigation strategies impact the makeup flow. Notably, within the CH_4-driven calcination scheme, a measurable demand for fresh $CaCO_3$ makeup only commences once the X exceeds a threshold of approximately 50% due to the significant deactivation mitigation. Accordingly, its correlation with the $CaCO_3$ makeup ratio r is still described by eqn (10), with the fitting constants updated to a_1 = 1.3626, f_1 = 0.3711, a_2 = 0.3215, f_2 = 0.4022, and b = 0.5090.

Fig. 11 illustrates the influence of X on the system's energy performance. As X increases from 10% to 50%, the solid circulation rate of the calcium loop decreases from 2460 mol s^{-1} to 474 mol s^{-1}. Since no fresh $CaCO_3$ makeup is required in this range, both the energy consumption for solid transport and the excess power demand of the calciner are reduced, leading to improved system efficiency. At X = 10%, the total power input is 120.55 MW, with a round-trip efficiency, energy efficiency, and exergy efficiency of 18.72%, 86.38%, and 83.25%, respectively. When X reaches 50%, the total power input decreases to 110.19 MW, while the round-trip, energy, and exergy efficiencies increase to 20.48%, 88.05%, and 85.04%, respectively. Beyond X = 50%, sorbent deactivation occurs, necessitating the addition of fresh $CaCO_3$. The required makeup amount increases with higher X, which elevates the calcination reaction's heat demand and raises the calciner's excess power consumption. The solid circulation rate declines, saving transport energy; however, this benefit is offset by the calciner's higher power demand. For instance, when X increases from 50% to 70%, the excess power for calcination rises from 107.84 MW to 114.71 MW. Consequently, the overall system efficiency slightly decreases beyond the 50% conversion threshold. At X = 70%, the round-trip, energy, and exergy efficiencies decline to 19.33%, 87.95%, and 84.81%, respectively.

Similar to the variations in system efficiency, the relationship between the specific energy consumption for carbon capture and X is shown in Fig. 11(c). As X increases from 10% to 50%, energy consumption declines from 9.05 MJ kg^{-1} to 8.41 MJ kg^{-1} due to reduced total system power input. Beyond this range, further increases in X cause higher power demand because of sorbent deactivation, raising energy consumption to 9.07 MJ kg^{-1} at X = 70%. Based on this energetic analysis, the system performs optimally at around a 50% conversion rate.

Fig. 12 illustrates the influence of X on the economic performance of the CaL-DRM-sCO_2 system. The most cost-sensitive components to variations in X are the calciner, the calci-

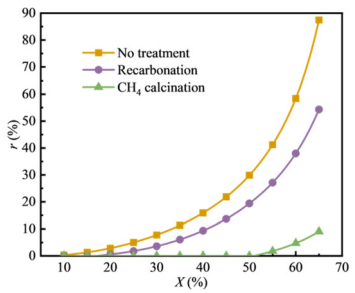

Fig. 10 Comparison of the $CaCO_3$ makeup ratio under different operational scenarios as a function of CaO conversion rate.

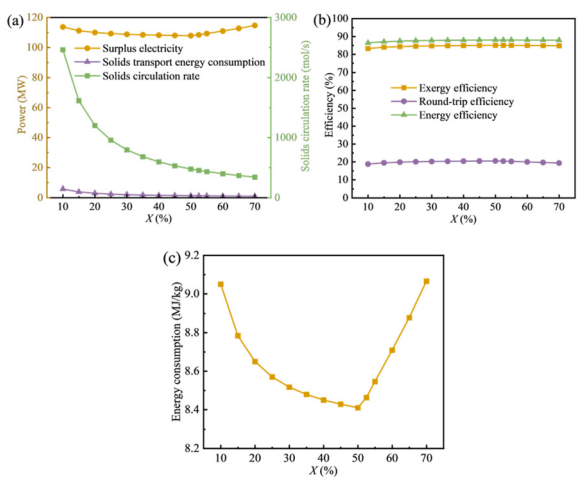

Fig. 11 Effect of CaO conversion rate (X) on the energetic performance of the CaL-DRM-sCO_2 system: (a) electrical power demand; (b) system efficiencies; (c) specific energy consumption for CO_2 capture.

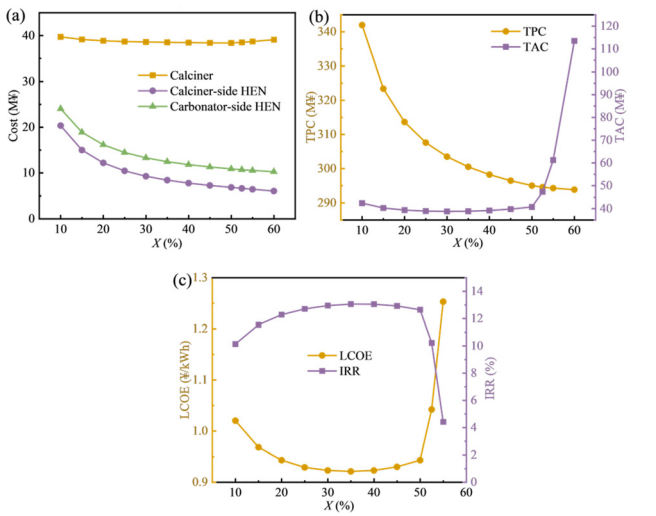

Fig. 12 Effects of CaO conversion (X) on the economic performance of the CaL-DRM-sCO_2 system: (a) equipment costs by component; (b) total investment cost; (c) LCOE and IRR.

ner-side HEN, and the carbonator-side HEN. As X increases from 10% to 50%, the heat load on the calciner-side and carbonator-side HENs gradually decrease, reducing their combined cost from 44.38 to 17.68 M¥. At the same time, the cost of the calciner drops from 39.72 to 38.37 M¥, leading to a downward trend in the total capital cost of the system. When X increases from 50% to 60%, the rising power demand causes the calciner cost to rise by 0.72 M¥. However, this increase is offset by a decrease of 1.44 M¥ in the HEN costs. As a result, the total equipment cost continues to decline as X increases.

As the TPC is proportional to the total capital cost, it decreases with increasing X, as shown in Fig. 12(b). The TPC declines from 341.98 M¥ to 293.82 M¥ as X rises from 10% to 60%. The overall trend of the TAC with increasing X is characterized by an initial gradual decrease due to reduced power demand, followed by a slow increase caused by higher limestone expenditure. Finally, when X exceeds 50%, the requirement for fresh limestone makeup drives a rapid escalation in TAC, which reaches 113.52 M¥ at X = 60%. It is evident that further increases in X beyond this point would lead to a sharp rise in the TAC, significantly impairing the system's economic viability.

Fig. 12(c) shows that the trend of LCOE closely follows that of TAC, indicating that TAC is the dominant factor influencing LCOE at a given X. In contrast, IRR exhibits a trend opposite to LCOE. As X increases from 10% to 35%, LCOE decreases from 1.02 ¥ per kWh to 0.92 ¥ per kWh, while IRR increases from 10.14% to 13.32%. When X further increases to 50%, LCOE rises slightly to 0.94 ¥ per kWh due to the elevated TAC, and IRR declines to 13.07%. Beyond this point, further increase in X leads to a severe deterioration in economic performance, making the project investment hardly profitable.

Based on a thorough analysis of X's impact on energy and economic performance, the ideal range for X is identified as 30%–50%. In this range, lower X values support economic growth, while higher values enhance energy efficiency.

4.2.2 Effects of heat exchanger minimum temperature. Fig. 13 illustrates the influence of the ΔT_{min} in the heat exchangers within the sCO_2 Brayton cycle on the energetic performance of the CaL-DRM-sCO_2 system. As the ΔT_{min} increases from 5 °C to 30 °C, the net power output decreases from 23.22 MW to 20.14 MW under constant power input conditions. This reduction is attributed to increased heat transfer losses and lower effectiveness in the sCO_2 heat exchangers, coupled with a decreased turbine inlet temperature, which collectively impair the expander's power generation capability. Consequently, the system round-trip efficiency declines from 21.06% to 18.27%, while the exergy efficiency decreases from 85.20% to 84.40%.

Fig. 14 illustrates the impact of the ΔT_{min} in the heat exchangers on the economic performance of the CaL-DRM-sCO_2 system. As the ΔT_{min} increases from 5 °C to 30 °C, major equipment costs, including the turbine, compressor, and recuperator—which contribute significantly to the total capital cost—all exhibit a decreasing trend, as shown in Fig. 14(a). At a ΔT_{min} of 5 °C, the costs of these components are 22.94 M¥, 21.14 M¥, and 36.73 M¥, respectively. When the ΔT_{min} increased to 30 °C, the costs decrease to 20.26 M¥, 16.41 M¥, and 15.40 M¥, respectively. This reduction can be attributed to two primary factors: the increase in the minimum temperature lowers the temperature of the sCO_2 working fluid after the heating section, thereby reducing the maximum cycle temperature. As a result, the power output of both the turbine and the compressor decreases, leading to lower equipment costs. Additionally, the required heat transfer area of the heat exchangers decreases with a larger temperature approach, which also contributes to the reduction in cost.

Meanwhile, the decrease in individual equipment costs results in a lower TPC, which then causes a slight drop in the TAC, as shown in Fig. 14(b). As the ΔT_{min} increases from 5 °C to 30 °C, the TAC slightly declines from 40.90 M¥ to 39.76 M¥. However, the unit operating cost for power generation rises with a larger temperature difference. This is due to the strong negative relationship between system power output and ΔT_{min}, as previously explained. Specifically, when ΔT_{min} increases

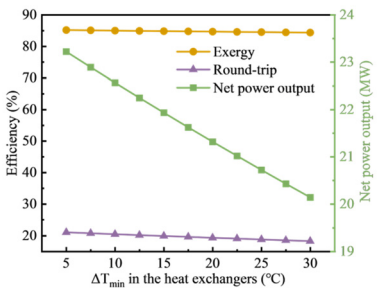

Fig. 13 Effect of the heat exchanger ΔT_{min} on the energetic performance of the CaL-DRM-sCO_2 system.

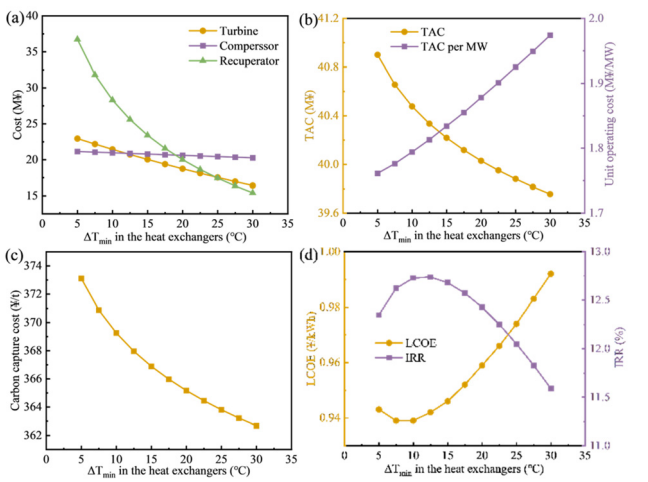

Fig. 14 Effect of the heat exchanger ΔT_{min} on the economic performance of the CaL-DRM-sCO_2 system: (a) major equipment costs; (b) TAC and unit operating cost of power generation; (c) CO_2 capture cost; (d) LCOE and IRR.

from 5 °C to 30 °C, the unit operating cost for power generation goes up from 1.761 M¥ per MW to 1.974 M¥ per MW.

Fig. 14(c) illustrates the influence of the ΔT_{min} on the carbon capture cost. The heat release from the carbonator remains constant, resulting in an unchanged system carbon capture rate and annual CO_2 capture capacity. Consequently, as the ΔT_{min} increases from 5 °C to 30 °C, the carbon capture cost follows the same trend as the TAC, decreasing slightly from 373.11 ¥ per t to 362.68 ¥ per t.

Fig. 14(d) shows the influence of the heat exchanger ΔT_{min} on the LCOE and IRR. The LCOE initially decreases and then increases with a rising ΔT_{min}, while the IRR exhibits the opposite trend. As the ΔT_{min} increases from 5 °C to 10 °C, the LCOE decreases from approximately 0.943 ¥ per kWh to 0.939 ¥ per kWh. This reduction occurs because the decline in TAC outweighs the decrease in net power output. Correspondingly, the IRR increases from 12.35% to 12.73%. However, when the ΔT_{min} further increases to 30 °C, the LCOE gradually rises to 0.99 ¥ per kWh and the IRR declines to 11.59%, indicating deteriorated economic performance. Thus, the optimal economic performance is achieved within a minimum temperature range of 5–10 °C.

In summary, both the system's energy and economic performance are favorable when the ΔT_{min} is relatively small. However, since very small values can cause significant technical challenges and uncertainties in practical engineering, a ΔT_{min} of 10 °C is recommended as the best balance.

4.2.3 Effects of system scale. The system scale, defined as the heat release rate of the carbonator during the energy discharge phase, is a key parameter influencing the system's economic performance. As shown in Fig. 15(a), the TPC increases with the system scale, but its growth rate gradually slows. When the scale increases from 10 MW to 20 MW, the TPC rises from 125.56 M¥ to 191.39 M¥, representing an increase of 65.83 M¥. When the scale expands by another 10 MW, the incremental increase in TPC drops to 54.87 M¥, demonstrating a clear economies-of-scale effect on cost. The unit capital cost for power generation also decreases with the expansion of the system scale, and the rate of decrease gradually diminishes. When the system scale increases from 1 MW to 10 MW, the unit capital cost decreases rapidly from 58.81 M¥ per MW to 22.23 M¥ per MW. As the scale further expands to 100 MW, the unit capital cost declines to 9.48 M¥ per MW.

The TAC also exhibits a pattern of diminishing growth with system scale, albeit more gradually compared to the TPC, as shown in Fig. 15(b). Specifically, when the system scale increases from 1 MW to 50 MW, the TAC rises from 1.49 M¥ to 50.07 M¥—an increase of 48.58 M¥. As the scale further expands to 100 MW, the TAC reaches 97.43 M¥, representing an incremental rise of 47.36 M¥. The unit operating cost for power generation also follows a step-like decreasing trend as the system scale enlarges. In the system scale range of 1–10 MW, the unit operating cost decreases rapidly from 2.64 M¥ per MW to 1.96 M¥ per MW, a reduction of 0.68 M¥ per MW. Beyond 10 MW, however, the rate of decrease slows significantly. By the time the scale reaches 100 MW, the cumulative reduction amounts to a mere 0.23 M¥ per MW.

As shown in Fig. 15(c), the LCOE follows the variation of the unit capital and operating costs, demonstrating clear economies of scale. When system capacity increases from 1 MW to 10 MW, the LCOE drops sharply from 2.37 to 1.23 ¥ per kWh; with further expansion, the decline becomes gradual, reaching 0.83 ¥ per kWh at 100 MW. In contrast, the IRR exhibits a mirror-image trend relative to LCOE. For capacities up to 3 MW, IRR is negative, indicating economic infeasibility. As capacity expands, IRR rises and exceeds the 6% benchmark discount rate at 11 MW (6.01%), marking the onset of positive returns; continued scale-up to 100 MW elevates IRR to 18.67%. Balancing these effects, a moderate installation size of approximately 40–70 MW is reasonable and can achieve superior techno-economic performance.

4.2.4 Effects of operational lifetime and utilization. The system's operating profile—comprising annual operating hours (utilization) and service lifetime—has a pronounced influence on techno-economic performance. The impact of annual operating hours is illustrated in Fig. 16. Both TAC and annual electricity revenue scale approximately linearly with utilization. As annual operating hours increase from 3000 h to 8000 h, TAC rises from 25.28 M¥ to 52.00 M¥ owing to the higher procurement cost of renewable electricity and the increased feedstock expenditure, corresponding to a rate of about 0.0053 M¥ per h. Over the same range, annual electricity revenue increases from 40.62 M¥ to 108.33 M¥ at roughly 0.0135 M¥ per h, substantially outpacing the growth of TAC. Consequently, higher utilization delivers net economic gains: LCOE decreases monotonically while IRR increases, as shown in Fig. 16(b). Specifically, when annual operating hours rise from 3000 h to 8000 h, LCOE declines from 1.38 ¥ per kWh to 0.81 ¥ per kWh, and IRR increases markedly from 3.14% to 18.97%. These results indicate low annual utilization is unlikely to yield positive investment returns.

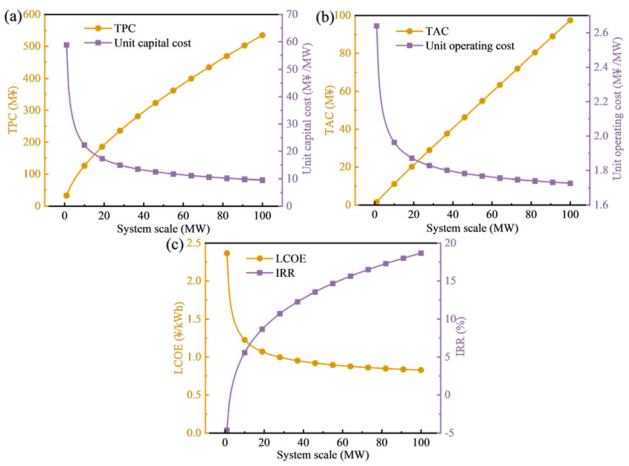

Fig. 15 Effect of the CaL-DRM-sCO_2 system scale on economic performance: (a) TPC and unit capital cost *vs.* capacity; (b) TAC and unit operating cost of power generation *vs.* capacity; (c) LCOE and IRR *vs.* capacity.

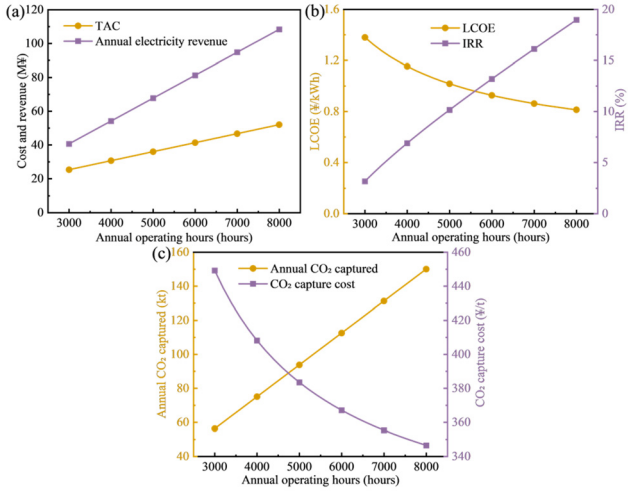

Fig. 16 Effects of annual operating hours on the CaL-DRM-sCO$_2$ system: (a) TAC and annual electricity revenue; (b) LCOE and IRR; (c) annual CO$_2$ captured and capture cost.

As shown in Fig. 16(c), annual CO$_2$ capture scales linearly with annual operating hours. When utilization increases from 3000 h to 8000 h, the captured CO$_2$ rises by 93.8 kt (*i.e.*, about 18.76 t h^{-1} for each additional operating hour). In parallel, the CO$_2$ capture cost declines with higher utilization: it drops from 449.20 ¥ per t-CO$_2$ at 3000 h to 346.53 ¥ per t-CO$_2$ at 8000 h. Taken together, annual operating hours are strongly and positively correlated with both economic and environmental performance. Nevertheless, continuous year-round operation is constrained by maintenance requirements and staffing. Within these practical limits, maximizing feasible annual operating hours enhances economic performance.

As shown in Fig. 17, extending the operational lifetime enhances techno-economic performance by amortizing upfront capital over a longer period. With a 20-year lifetime, the LCOE is 1.00 ¥ per kWh and the IRR is 11.64%; when the lifetime is extended to 60 years, the LCOE decreases to 0.89 ¥ per kWh and the IRR increases to 13.08%, strengthening investment returns. Nevertheless, lifetime extension must account for whole-life dynamics: equipment aging may raise repair frequency and operation and maintenance expenditures, and rapid technology turnover can induce performance degradation and obsolescence risks. Hence, lifetime should not be pushed arbitrarily long; it should be selected by balancing initial capital expenditures, escalation of operation and maintenance costs, overhaul/replacement strategies, and technology currency to maximize life-cycle economic value.

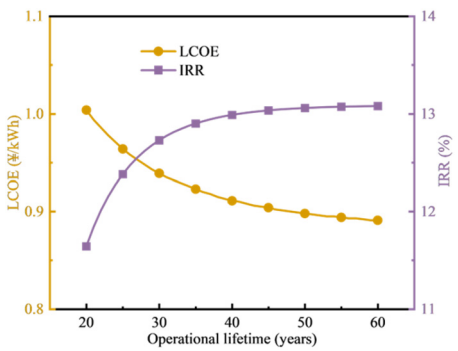

Fig. 17 Effect of operational lifetime on techno-economic performance of the CaL-DRM-sCO$_2$ system: LCOE and IRR.

5. Conclusions

This work proposes a CaL-DRM-sCO$_2$ system. The CH$_4$ atmosphere lowers the calcination temperature by about 200 °C, mitigates sorbent deactivation, and reacts *in situ* with the released carbon dioxide to co-produce synthesis gas, while the carbonation stage enables approximately 90% CO$_2$ capture. Multi-objective optimization reveals clear efficiency–cost trade-offs:

The Pareto-optimal compromise yields an exergy efficiency of 85.03% at a levelized cost of electricity of 0.94 ¥ per kWh for a 40 MW plant, with the power block simplified to a recuperated cycle configuration. Under these conditions, the net electric output reaches 22.57 MW, corresponding to a round-trip electrical efficiency of 20.47%. When credit is given to the synthesis-gas co-product and ~90% carbon dioxide capture, the overall system efficiency rises markedly to 88.04%, with a specific capture energy of 8.41 MJ per kg-CO$_2$.

An operating window with 30–50% CaO conversion, combined with a 10 °C minimum temperature in the recuperators, yields favorable thermo-economic performance.

As plant capacity expands from 1 to 100 MW, the levelized cost of electricity declines sharply from 2.37 to 0.83 ¥ per kWh. A capacity range of 40–70 MW appears most practical when considering both investment scale and associated risks. Moreover, higher annual utilization further enhances economics, reducing the LCOE to 0.81 ¥ per kWh and boosting the internal rate of return to 18.97%.

The present analysis relies on steady-state models employing zero-dimensional reactor representations and cost correlations. Future work should extend beyond these simplifications to incorporate detailed reaction kinetics and multi-scale coupling, dynamic operation and dispatch optimization, long-term sorbent cycling and regeneration strategies, pilot-scale validation, and comprehensive assessment of methane supply-chain leakage on life-cycle performance.

Conflicts of interest

There are no conflicts to declare.

Data availability

This paper is a methodological study and does not utilize any specific datasets. The code is available in the GitHub repository: gitee.com/sun-zihao/nbCaLtrees-zh.

Supplementary information (SI) is available. See DOI: https://doi.org/10.1039/d5eb00225g.

Acknowledgements

This work is supported by National Key Research and Development Program of China (no. 2024YFE0212800).

References

1 I. R. E. Agency, *Renewable power generation costs in 2022*, Abu Dhabi, United Arab Emirates, 2023.
2 I. E. Agency, *Net Zero by 2050: A Roadmap for the Global Energy Sector*, Paris, France, 2021.
3 A. Toktarova, L. Gruber, M. Hlusiak, D. Bogdanov and C. Breyer, *Int. J. Electr. Power Energy Syst.*, 2019, **111**, 160–181.
4 Y. Wang, R. Wang, K. Tanaka, P. Ciais, J. Penuelas, Y. Balkanski, J. Sardans, D. Hauglustaine, W. Liu, X. Xing, J. Li, S. Xu, Y. Xiong, R. Yang, J. Cao, J.-M. Chen, L. Wang, X. Tang and R. Zhang, *Nature*, 2023, **619**, 761–767.
5 H. Jiang, L. Yao, J. Qin, Y. Bai, M. Brandt, X. Lian, S. J. Davis, N. Lu, W. Zhao, T. Liu and C. Zhou, *Nat. Commun.*, 2025, **16**, 4523.
6 I. Sarbu and C. Sebarchievici, *Sustainability*, 2018, **10**(1), 191.
7 E. Borri, A. Tafone, A. Romagnoli and G. Comodi, *Energy Convers. Manage.*, 2017, **143**, 275–285.
8 G. Feng, Y. Li, X. Cheng, B. Hou, D. Qu, R. Xu and L. Zhang, *Therm. Power Gener.*, 2024, **53**, 1–9.
9 A. H. Abedin and M. A. Rosen, *Energy*, 2012, **41**, 83–92.
10 P. Pardo, A. Deydier, Z. Anxionnaz-Minvielle, S. Rougé, M. Cabassud and P. Cognet, *Renewable Sustainable Energy Rev.*, 2014, **32**, 591–610.
11 H. Liu, Y. Zhang, Q. Xu, W. Han and J. Shen, *Appl. Energy*, 2025, **377**, 124535.
12 R. Chacartegui, A. Alovisio, C. Ortiz, J. M. Valverde, V. Verda and J. A. Becerra, *Appl. Energy*, 2016, **173**, 589–605.
13 C. Ortiz, J. M. Valverde, R. Chacartegui, L. A. Perez-Maqueda and P. Giménez, *Renewable Sustainable Energy Rev.*, 2019, **113**, 109252.
14 Q. Xu, l. Wang, Z. Li and L. Shi, *Energy Convers. Manage.*, 2023, **276**, 116592.
15 S. E. B. Edwards and V. Materić, *Sol. Energy*, 2012, **86**, 2494–2503.
16 C. Ortiz, R. Chacartegui, J. M. Valverde, A. Alovisio and J. A. Becerra, *Energy Convers. Manage.*, 2017, **149**, 815–829.
17 C. Zhang, J. Sun, Y. Qiao and J. Wei, *Energy*, 2024, **312**, 133687.
18 L. Teng, Y. Xuan, Y. Da, X. Liu and Y. Ding, *Energy Storage Mater.*, 2020, **25**, 836–845.
19 D. Wang, Z. Sun, Q. Xu, R. Tian, W. Han and J. Shen, *Energy Convers. Manage.*, 2024, **318**, 118888.
20 P. Sun, J. R. Grace, C. J. Lim and E. J. Anthony, *AIChE J.*, 2007, **53**, 2432–2442.
21 M. Benitez-Guerrero, J. M. Valverde, P. E. Sanchez-Jimenez, A. Perejon and L. A. Perez-Maqueda, *Sol. Energy*, 2017, **153**, 188–199.
22 M. E. Diego, B. Arias, G. Grasa, J. C. Abanades, L. Díaz, M. Lorenzo and A. Sánchez-Biezma, *Energy Procedia*, 2014, **63**, 2060–2069.
23 Z. He, Y. Li, W. Zhang, X. Ma, L. Duan and H. Song, *Energy Convers. Manage.*, 2017, **148**, 1468–1477.
24 R. Anwar, A. Al Kape, M. Lusi, E. Voutsas, A. Cammarata, A. Rafferty and M. V. Sofianos, *J. Energy Storage*, 2025, **114**, 115784.
25 H. Guo, X. Kou, Y. Zhao, S. Wang, Q. Sun and X. Ma, *Chem. Eng. J.*, 2018, **334**, 237–246.
26 I. Wang, S. Huang, S. Wang, X. Bie, H. Zhou and Z. Li, *Sep. Purif. Technol.*, 2024, **333**, 125975.
27 L. Teng, Y. Xuan, Y. Da, C. Sun, X. Liu and Y. Ding, *Chem. Eng. J.*, 2022, **440**, 135955.
28 B. Shao, Y. Zhu, J. Hu, Y. Zong, Z. Xie, S. Li, W. Du, M. Wang, H. Liu and F. Qian, *Chem. Eng. J.*, 2024, **483**, 149098.
29 U. Tesio, E. Guelpa and V. Verda, *Energy Convers. Manage.: X*, 2020, **6**, 100038.
30 L. Zhen-shan, C. Ning-sheng and E. Croiset, *AIChE J.*, 2008, **54**, 1912–1925.
31 S. Michalski, D. P. Hanak and V. Manovic, *J. Cleaner Prod.*, 2019, **219**, 540–551.
32 U. Tesio, E. Guelpa, C. Ortiz, R. Chacartegui and V. Verda, *Energy Convers. Manage.: X*, 2019, **4**, 100025.
33 S. Khosravi, S. Hossainpour, H. Farajollahi and N. Abolzadeh, *Energy*, 2022, **240**, 122466.
34 *Summary of the Sandia Supercritical CO_2 Development Program. [electronic resource]*, Washington, D.C.: United States. National Nuclear Security Administration; Oak Ridge, Tenn.: distributed by the Office of Scientific and Technical Information, U.S. Dept. of Energy, 2011.
35 U. Tesio, E. Guelpa and V. Verda, *Energy Convers. Manage.: X*, 2020, **6**, 100039.
36 N. T. Weiland, B. W. Lance and S. R. Pidaparti, "sCO2 Power Cycle Component Cost Correlations From DOE Data Spanning Multiple Scales and Applications." proceedings of the ASME Turbo Expo 2019: Turbomachinery Technical Conference and Exposition, Volume 9: Oil and Gas Applications; Supercritical CO2 Power Cycles; Wind Energy, Phoenix, Arizona, USA, June 17–21, 2019, V009T38A008, ASME. https://doi.org/10.1115/GT2019-90493.
37 M. D. Carlson, B. M. Middleton and C. K. Ho, V001T05A009 T1 - Techno-Economic Comparison of Solar-Driven SCO2 Brayton Cycles Using Component Cost Models Baselined With Vendor Data and Estimates VL - DO - 10.1115/ES2017-3590 ER, 2017.
38 Y. Zhang, H. Liu, J. Lu, Q. Xu and C. Xu, *J. Energy Storage*, 2025, **130**, 117487.